HHS Public Access

Author manuscript

ACS Nano. Author manuscript; available in PMC 2023 April 28.

Published in final edited form as:

ACS Nano. 2022 December 27; 16(12): 20340–20352. doi:10.1021/acsnano.2c06275.

Innate Immune Stimulation using 3D Wireframe DNA Origami

Rebecca R. Du[1], **Edward Cedrone**[2], **Anna Romanov**[1,3], **Reuven Falkovich**[1], **Marina A. Dobrovolskaia**[2], **Mark Bathe**[1,*]

[1]Department of Biological Engineering, Massachusetts Institute of Technology, Cambridge, MA 02139, USA

[2]Nanotechnology Characterization Laboratory, Cancer Research Technology Program, Frederick National Laboratory for Cancer Research, Frederick, MD 21702, USA

[3]Koch Institute for Integrative Cancer Research, Massachusetts Institute of Technology, Cambridge, MA 02139, USA

Abstract

3D wireframe DNA origami have programmable structural and sequence features that render them potentially suitable for prophylactic and therapeutic applications. However, their innate immunological properties, which stem from parameters including geometric shape and CpG content, remain largely unknown. Here, we investigate the immunostimulatory properties of 3D wireframe DNA origami on the TLR9 pathway using both reporter cell lines and primary immune cells. Our results suggest that bare 3D polyhedral wireframe DNA origami induce minimal TLR9 activation despite the presence of numerous internal CpG dinucleotides. However, when displaying multivalent CpG-containing ssDNA oligos, wireframe DNA origami induce robust TLR9 pathway activation, along with enhancement of downstream immune response as evidenced by increases in Type I and Type III IFN production in peripheral blood mononuclear cells. Further, we find that CpG copy number and spatial organization each contribute to the magnitude of TLR9 signaling, and that NANP-attached CpGs do not require phosphorothioate stabilization to elicit signaling. These results suggest key design parameters for wireframe DNA origami that can be programmed to modulate immune pathway activation controllably for prophylactic and therapeutic applications.

Keywords

3D wireframe DNA origami; TLR9; CpG; multivalency; immunostimulation; immunomodulation

Over the past several decades, the field of nucleic acid nanotechnology has enabled the fabrication of programmable DNA-based assemblies of prescribed size, geometry,

*Address correspondence to mark.bathe@mit.edu.

ASSOCIATED CONTENT: This work has previously been submitted as a pre-print to bioRxiv: Du, R. R.; Cedrone, E; Dobrovolskaia, M; Bathe, M. Innate Immune Stimulation using 3D Wireframe DNA Origami. **2022**, 2022.07.08.499376. *bioRxiv*. https://doi.org/10.1101/2022.07.08.499376.

SUPPORTING INFORMATION: Additional methods for supporting figures; additional structural characterization of DNA NANPs; additional reporter cell and PBMC results and figures; DNA NANP stability assay; DNA NANP confocal imaging results; tables containing complete lists of scaffold and staple sequences for DNA NANP assembly (DOCX).

rigidity, and chemical composition.[1–10] These nanomaterials now comprise a toolbox for the design and fabrication of nanodevices capable of interacting with diverse cellular environments.[11–13] One class of discrete nucleic acid nanoparticles (NANPs) is scaffolded DNA origami, which are folded by the hybridization of short, single-stranded DNA staples to programmed complementary regions on a long, single-stranded DNA scaffold. These NANPs can be fabricated on the 10–100nm scale known to be advantageous for prolonged blood circulation half-life,[14] tumor permeability,[15] and lymph trafficking,[16] though chemical stabilization to increase serum half-life is required for some applications due to nuclease activity.[17,18] Since the introduction of DNA origami by Paul Rothemund,[19] who used this approach to pioneer the fabrication of 2D rectilinear, bricklike assemblies of parallel DNA duplexes, DNA origami design has been generalized to enable the synthesis of 2D and 3D wireframe assemblies to fabricate arbitrary polyhedral geometries, including virus-like geometries.[1,3–5,9] Furthermore, the recent development of fully automated sequence design algorithms such as DAEDALUS, TALOS, vHelix, and ATHENA[1,4,5,9] has facilitated the design and fabrication of wireframe structures composed of dual-duplex or six-helixbundle edges with variable mechanical properties, allowing for the production of virus-like and other geometries for diverse biophysical and cellular applications.[1–4,8,9] Scalable scaffold production strategies using M13 bacteriophage engineering and bioproduction have also now enabled control over scaffold sequence composition and length, expanding the accessible design space for wireframe NANPs.[20–22]

The ability to chemically functionalize NANPs permits the attachment of therapeutic nucleic acid cargo such as siRNA and miRNA, as well as small molecules, aptamers, peptides, and proteins with nanometer-level spatial control. This enables them to perform functions such as active targeting or immune cell stimulation,[11,13,23] thereby enhancing the potential for NANPs to interface with biological systems *in vitro* and *in vivo*. [24–26] Furthermore, the intrinsic immunostimulatory properties of NANPs used for such applications may contribute crucially to their function as well. For example, strongly pro-inflammatory NANPs may be well-suited for vaccine development, and conversely, minimally immunostimulatory NANPs may be advantageous for therapeutic applications in which evasion of innate immune stimulation is desired. However, the immunostimulatory properties of different classes of NANPs may vary greatly, and while several studies have been undertaken in this direction in recent years,[27–34] the intrinsic immunostimulatory properties of 3D wireframe DNA NANPs, as well as their ability to controllably modulate the innate immune response, have yet to be elucidated.

The innate immune system contains several pattern recognition receptors (PRRs) that are responsible for recognizing evolutionarily conserved pathogen-associated or damage-associated molecular patterns (PAMPs or DAMPs). Once bound to their ligands, these PRRs trigger signaling through one of several convergent pathways to initiate innate immune activation while simultaneously priming the adaptive immune response.[35,36] Binding of PRRs to their corresponding ligand triggers activation of downstream signaling pathways, ultimately resulting in the production of Type I interferons (IFNs) and other pro-inflammatory cytokines that are essential to the initiation of a host of immune functions.[37,38]

Toll-like Receptors (TLRs) are a family of transmembrane PRRs that sense and respond to a wide variety of pathogen- or damage-associated ligands, including nucleic acids. TLRs are composed of a N-terminal PAMP-binding ectodomain, a transmembrane domain and a C-terminal Toll IL-1 receptor domain (TIR) and are subdivided into two groups according to whether they localize at the cell surface membrane or within the endosomal membrane.[39,40] The endosomal TLR subfamily, which consists of TLR3, TLR7/8, and TLR9, is involved in nucleic acid recognition, where TLR3 and TLR7/8 recognize dsRNA and ssRNA, respectively, and TLR9 responds to single-stranded DNA (ssDNA) containing unmethylated cytosine-phosphate-guanine dinucleotides (CpGs).[41–43] Each of the monomers within the TLR9 homodimer undergoes a conformational change upon binding to a CpG-containing ssDNA oligo, enabling the formation of a 2:2 TLR9 monomer:CpG oligo complex in which each monomer interacts with both CpGs.[44,45] Activated TLR9 homodimer formation brings the two C-terminal TIR domains into close proximity, allowing for the assembly of the TIR-containing adaptor protein (TIRAP) and MyD88 adaptor protein-containing myddosome complex, the initiation of a downstream signaling cascade, and the eventual production of Type I IFNs and pro-inflammatory cytokines.[44,46–48]

In recent years, the success of immune checkpoint inhibitors in the treatment of cancers has stimulated widespread interest in harnessing the therapeutic potential of not just adaptive immune pathways but also the innate immune system. As PRRs such as TLR9 are critical contributors to the innate immune response, this has prompted investigations into the application of TLR9 agonists as anti-cancer drugs, vaccine adjuvants, and combination therapies, a few of which, such as MGN-1703 and SD-101, are in ongoing clinical development.[49–53] While many of these agonists consist of functionalized oligonucleotides with optimized CpG motifs, or CpG dinucleotides placed within a particular sequence context that enhances the potency of TLR9 activation, several DNA-based nanostructures have been used to stimulate innate immune signaling through TLR activation as well.[28–30,34,54]

For example, the Liedl group[28] placed CpG oligos onto immune inert DNA origami tubes to induce CpG-dependent cytokine production and immune cell activation. In the same year, Li *et al.* found that small self-assembled DNA tetrahedra functionalized at their vertices with CpG motifs could induce enhanced secretion of inflammatory cytokines via activation of the TLR9 pathway.[30] More recently, the Ding group[34] developed a cancer vaccine nanodevice in which CpG loops were hybridized within an antigen-displaying DNA origami tube to enable TLR9 activation following pH-triggered conformational change of DNA locks. And most recently, Comberlato *et al.* fixed CpG dimer pairs at distances of 7nm or 38nm on a 2D nano-disk and showed that the 7nm dimer pair, which matched the distance between binding sites in the TLR9 dimer, induced significantly increased immune activation compared with the 38nm dimer pair, demonstrating the importance of effective spatially controlled ligand presentation.[29] However, this study was limited to dimer CpGs, whereas TLR9 signaling is thought to be dependent not just on binding of individual TLR9 dimers but also on the formation of activated dimer clusters. NANPs offer the distinct opportunity to control both valency and spatial positioning of multivalent CpG ligands to investigate their impacts on TLR9 activation.

Previous studies using non-DNA nanotechnologies have also demonstrated that incorporating CpGs into nanoparticles can influence the type of induced immune response.[55–60] However, these studies were limited by the inability to precisely control nanometer-scale spatial positioning and stoichiometry, so the effects of these parameters on TLR9 activation remain poorly understood. Additionally, although Hong *et al.* identified the primary properties of structured DNA assemblies involved in immunological recognition[31] and Schüller *et al.* demonstrated that nonfunctionalized DNA origami tubes did not trigger cytokine production or induce dendritic cell (DC) activation,[28] the immunostimulatory properties of unmodified wireframe DNA origami and the contributions of physical parameters including sequence composition and geometry remain unknown.

Here, to address the aforementioned gaps in knowledge, we characterized the immunological properties of unmodified 3D wireframe DNA origami by first examining the effects of NANP geometry and structuring on the TLR9 pathway in isolation using TLR9 reporter cells. We then engineered NANPs displaying discrete copy numbers of CpG oligos with precise spatial organizations to reveal how CpG valency, inter-CpG distancing, and spatial presentation each influence the magnitude of TLR9 activation. Finally, we tested these engineered NANPs in peripheral blood mononuclear cells (PBMCs) to investigate the overall impact of these immunomodulatory constructs within the more complex, physiologically relevant environment of a mixed population of multiple immune cell subtypes. Our study reveals design principles that may help engineer NANPs for programmable immunostimulation in prophylactic and therapeutic applications.

RESULTS AND DISCUSSION

Design and characterization of wireframe DNA nanoparticles

Wireframe DNA origami nanoparticles were designed with DAEDALUS[9] and folded from a bacterially-produced synthetic circular scaffold with a tenfold excess of single-stranded DNA staples via thermal annealing.[22] In order to characterize the immunostimulatory properties of bare and CpG-modified NANPs, which are composed of dual-duplex DNA edges and additionally contain 262 CpG dinucleotides randomly distributed throughout the scaffold and staples (Table S1), we focused on multiple variations of one primary NANP, a pentagonal bipyramid with 84 base pairs per edge (PB84) with an edge length of approximately 28nm. As a comparative construct to investigate the effects of geometry on TLR9 and cGAS-STING activation, we additionally fabricated an icosahedron with 42 base pairs per edge (ICO42) with an edge length of approximately 14nm, which was designed using the same scaffold as PB84 to eliminate the potential effects of sequence variation on innate immune signaling (Figure 1A). In addition to the bare NANPs that we used to probe the intrinsic immunogenicity of these wireframe structures, we also fabricated PB84 and ICO42 constructs with 20-nt single-stranded overhangs on the 3’ end of select staples (Figure 1, Figure S1). These overhang sequences comprised the commercially available TLR9 agonist oligodeoxynucleotide (ODN) 2006/7909, a class B CpG ODN containing three repeats of an optimized hexamer known to strongly activate human TLR9.[41,61] We used this approach to display CpG motifs multivalently at defined spatial locations on our NANP constructs in order to interrogate the effects of CpG copy number, spacing, and

organization on TLR9 activation (Figure 1B). Variations of the CpG overhangs, specifically phosphorothioated and CpG-free sequences, were designed as comparative controls and displayed on NANPs as well (Figure 1B). Validation of proper NANP self-assembly was first performed using agarose gel electrophoresis. Successful folding was indicated by an upward shift of the folded NANP band relative to the scaffold band, and the addition of ssDNA overhangs enhanced the magnitude of the shift (Figure 1C, Figure S1). NANP monodispersity was further characterized using dynamic light scattering (DLS), and the hydrodynamic diameter of each sample was measured to validate batch-to-batch consistency in NANP folding (Figure 1D, Figure S2). Fluorimetry using Cy5-labeled oligos hybridized to the CpG overhangs confirmed that this approach presented the expected copy numbers of CpGs on each NANP variant (Figure S3). To characterize the stability of NANPs with CpG overhangs in cell assay conditions, NANPs were incubated in tissue culture media for up to 24 hours and assessed using gel shift analysis (Figure S4). A gel clot endotoxin test was used to verify that the endotoxin level of each sample was below a threshold of 1.5 EU/mL prior to its application in cell assays.

Effects of unmodified DNA nanoparticles on TLR9 pathway activation

We first sought to characterize the baseline immunostimulatory properties of NANPs by investigating the effects of unmodified PB84 and ICO42 on TLR9 pathway activation using reporter cell lines. Consistent with previous findings,[31] wireframe NANPs that were not complexed with lipofectamine prior to incubation with reporter cells failed to elicit a significant innate immune response, potentially due to a lack of internalization (Figure S5). Thus, for all experiments described herein, all constructs were co-complexed with lipofectamine to enable uniform internalization. Additionally, to investigate whether lipofectamine-complexed NANPs traffic as anticipated, we performed confocal microscopy and found that NANPs were effectively internalized into reporter cells and colocalized with late endosomes and lysosomes, where TLR9 is expressed (Figure S6). HEK-Blue reporter cells expressing stably transfected human TLR9 (HEK-Blue TLR9 cells) were incubated with 10nM PB84 and ICO42, and to assess the relative impacts of NANP structuring, we compared equivalent concentrations of the scaffold (phPB84) as well as the PB84 and ICO42 staple sets as non-structured controls. After incubation of TLR9 reporter cells with all NANP samples for 24 hours, we evaluated TLR9 activation, reported as an increase in absorbance, and found that structured constructs resulted in minimal activation of the TLR9 pathway. Interestingly, the unstructured ssDNA scaffold induced only slightly higher levels of TLR9 activation (Figure S7), even though the NANP scaffold and staple sets contained several hundred CpG dinucleotides, as noted above. While only three sets of these CpG dinucleotides would be classified as strongly stimulatory CpG motifs based on previously identified sequence requirements,[52,53] our result nevertheless suggests that the numerous CpG dinucleotides within the scaffold and folded nanostructures may be less accessible to TLR9 binding than otherwise anticipated. The effects of nanostructuring on shielding immunostimulatory motifs such as CpGs from innate immune recognition may therefore be an interesting question for further investigation in future work.

To verify that the observed responses to these NANPs were indeed mediated by the TLR9 pathway, we performed the same set of experiments in the parental Null 1 cell line, which does not express TLR9 (Figure S8), revealing that all formulations failed to elicit a response.

Designing DNA nanoparticles for variable immunostimulation

We next investigated the ability of 3D wireframe DNA NANPs to trigger programmable activation of the innate immune response through rationally designed display of immunostimulatory motifs. Since we did not observe significant stimulation of the TLR9 pathway by unmodified structured PB84, we reasoned that we could treat this structure as immunologically inert in the context of this TLR9 reporter cell line. This NANP could then be controllably functionalized with immunostimulatory motifs to systematically investigate the relative impacts of various parameters governing nanoscale display, specifically CpG copy number, inter-CpG spacing, and CpG spatial organization including surface accessibility, without confounding levels of baseline TLR9 activation.

To this end, we fabricated PB84 variants displaying 0, 10, 20, or 40 copies of CpG-OH distributed evenly across the exterior of the NANP (Figure 1B). Nanoparticles displaying corresponding copy numbers of CpG-free overhangs (CpG-f-OH) of identical length and GC content served as comparative controls. We transfected each of these formulations into HEK-Blue TLR9 cells, and following a 24-hour incubation period, we verified that PB84 displaying 0 copies of CpG-OH did not activate TLR9. In contrast, each of the constructs displaying 10, 20, or 40 copies of CpG-OH were able to induce TLR9 activation, where increasing CpG-OH copy number on the nanostructure led to monotonic increase in TLR9 activation (Figure 2A, Figure S9). Importantly, the total concentration of CpG motifs was held constant for each sample (Figure 2A), indicating that the magnitude of TLR9 activation is dependent on one of the parameters that was changing across samples, such as the valency of CpG motifs per NANP, rather than concentration. We also found that all constructs displaying CpG-f-OH, regardless of copy number per NANP, did not induce significantly higher levels of TLR9 activation compared with the unmodified nanostructure, which showed that changes in non-CpG-containing total DNA content have no effect on TLR9 signaling (Figure S10). To test whether this method of controllable immunostimulation was applicable to more than a single type of NANP, we also fabricated ICO42 displaying 0, 10, 20, or 30 copies of CpG-OH. As with PB84, we observed that the magnitude of TLR9 activation was dependent on the copy number of CpG-OH presented by the NANP (Figure 2B). However, the magnitudes of TLR9 pathway activation by the ICO42 and PB84 constructs displaying identical copy numbers of CpG-OH was different, suggesting that different NANP geometries may also influence TLR9 activation levels through differences in spatial organization of CpG overhangs on the NANP surface.

Investigating parameters controlling DNA nanoparticle-mediated immune activation

Because NANP structuring significantly affects the intensity of TLR9 signaling, we further investigated the impact of CpG attachment to NANPs on TLR9 activation. As precise control over directionality and spatial positioning is one distinct advantage of wireframe DNA origami with regards to other nanomaterials, we began by testing whether the orientation of CpG-OH presentation on NANPs affected TLR9 activation. Interestingly, we

found that there were no significant differences in TLR9 signaling between PB84 constructs displaying CpG-OHs towards the exterior versus towards the interior of the NANP (Figure S11). This may be the result of the flexibility of the 20-nt ssDNA overhang and the porous wireframe structure of wireframe NANPs: because only the duplex edges are solid, the 3' terminus of the inward-facing overhangs may in fact end up on the exterior of the NANP. To further investigate the contribution of the NANP itself to TLR9 activation, we compared TLR9 activation induced by identical concentrations of free versus NANP-attached CpG-OHs. We found that there was no TLR9 signaling in response to free CpG-OHs at any of the tested concentrations, whereas the same concentrations of CpG-OH displayed on NANPs induced strong TLR9 activation (Figure S12).

To test whether this lack of activation was due to degradation of free CpG-OHs by intracellular DNases, we incubated HEK-Blue TLR9 cells with phosphorothioate-stabilized free CpG-OHs (pCpG-OHs). Unlike the non-stabilized CpG-OHs, the magnitude of TLR9 activation was correlated with the concentration of pCpG-OHs delivered, as anticipated (Figure S12). Interestingly, we found that when CpG-OHs were displayed on NANPs, they were able to induce similar levels of TLR9 activation as their free pCpG-OH counterparts. These results suggest that attachment of CpG-OHs to DNA nanoparticles produces a similar effect to phosphorothioate stabilization of CpG oligos alone, implying that either NANP-bound CpG-OHs may be less susceptible to DNase degradation, or that the effects of NANP-mediated CpG-OH clustering may be able to compensate for the limited stability of phosphodiester CpG overhangs. Lastly, we tested the effects of proximity between the CpG motif and the NANP by varying the CpG location along the ssDNA overhang. For the set of distances and NANPs explored here, we found that constructs where the CpG motif was furthest away from the NANP induced significantly higher levels of TLR9 activation compared to NANPs where the CpG motif was spatially closer along the ssDNA overhang (Figure S13A). This suggests that these NANPs may provide a steric hindrance towards CpG-TLR9 binding when there is insufficient distance between the dual-duplex edge of the NANP and the CpG motif, which highlights spatial distancing between the NANP and the CpG as another parameter that might influence the magnitude of TLR9 activation. Interestingly, a previous study demonstrated that attachment of dsDNA linkers between CpG oligos and the base DNA nanostructure resulted in TLR9 activation levels which decreased proportionally with increasing linker length, highlighting what they described as 'low spatial tolerance' for CpG-TLR9 binding.[29] Our results corroborate these findings and suggest that as the flexibility of the CpG oligo increases or decreases past a certain point, the efficacy of precise spatial presentation is reduced.

In the preceding assays, CpG-OH valency, inter-CpG distance, and spatial organization were all variable across the NANPs tested. To reduce the complexity of the system, we held CpG-OH copy number constant and analyzed the effects of the remaining parameters on the TLR9 pathway. Based on the crystal structure of activated TLR9 bound to CpG oligos,[45] we and others[29] measured the distance between CpG binding domains within the TLR9 dimer to be ~7nm, which has also been shown to be optimal for TLR9 activation. To test the role of this spacing within the context of wireframe origami NANPs, we fabricated three PB84 constructs, each displaying 10 copies of CpG-OH with distances between adjacent CpG overhangs varying from 7nm to 20nm (Figure 3A). Upon transfecting these samples

into HEK-Blue TLR9 cells, we observed that the NANP in which adjacent CpG-OHs were positioned 7nm apart induced a significantly higher level of TLR9 activation compared to constructs with 14 and 20 nm CpG-OH spacing, consistent with prior observations of TLR9 activation exhibiting step-like behavior at 7nm.[29]

Next, to investigate the impact of the spatial distribution of CpG-OHs across the 3D surface of NANPs on TLR9 signaling, we synthesized PB84 constructs with five CpG-OHs displayed at low, medium, and high clustering densities on either one or both sides of the NANP. Interestingly, although the distance between adjacent CpG overhangs were 10nm and 25nm for the highest and lowest clustering density structures, respectively, we saw no significant difference between the magnitude of TLR9 activation induced by any of the five CpG-OH constructs (Figure 3B). In agreement with a previous report,[29] this may suggest that TLR9 binding has a low tolerance for CpG oligos displayed at sub-optimal distances greater than 7nm apart. Additionally, we found that there was a significant difference in TLR9 signaling between each of the five CpG-OH constructs tested and their corresponding 10 CpG-OH counterparts, even though the total CpG concentration and inter-CpG distances were held constant for each pair of NANPs. This suggests that the presentation of CpG overhangs on both sides of the NANP enhanced TLR9 binding relative to a single-sided CpG display examined previously.[29] As previous studies showed that clustering multiple activated TLR dimers in close proximity mediated enhanced downstream signaling,[62,63] the 10 CpG-OH constructs may be able to coordinate binding of more dimers than their five CpG-OH counterparts, thereby increasing the strength of NANP-mediated TLR9 activation. Additionally, different magnitudes of TLR9 activation were observed in response to these NANPs compared to constructs in which all 10 overhangs were displayed on the same side of the NANP, suggesting that it is not only valency and inter-CpG spacing that affects TLR9 activation, but the spatial distribution of these overhangs as well.

Because we had preliminary evidence that the geometry of the NANP, which impacts CpG spatial organization, affects TLR9 activation (Figure 2), we folded several NANPs of different shapes from the same phPB84 scaffold and attached CpG overhangs to each NANP, ensuring that the distance between each pair of adjacent CpGs on every edge was fixed at 7nm (Figure 3C). When these constructs were transfected into HEK-Blue TLR9 cells, we found that while NANPs with similar geometries induced similar levels of TLR9 activation, there was a significant difference between the TLR9 response towards NANPs with very different geometries, such as the tetrahedron and the icosahedron. This suggests that NANP geometry is yet another parameter that influences the potency of TLR9 activation.

Interferon response towards immunostimulatory DNA NANPs in primary cells

To investigate whether the preceding NANP-induced immune pathway modulation of immune pathway activation translated from reporter cell lines to primary cells, we evaluated the impact of NANPs on cytokine and interferon induction in human PBMCs. PB84 displaying 0, 20, and 40 copies of CpG-OH were transfected into PBMCs, where the total concentration of CpG-OHs in the 20 and 40 CpG-OH samples was held constant at 100nM. After incubation for 24 hours, the immunostimulatory activity of each construct was quantified using a multiplexed enzyme-linked immunosorbent assay (ELISA) to

measure secretion of IFNα, IFNβ, IFNω, and IFNλ, interferons which are known to be expressed in response to intracellular nucleic acids, as well as pro-inflammatory cytokines IL-6, IL-12, and TNF-α.[35,36] While expression levels of the pro-inflammatory cytokines tested were minimal (Figure S14), we found strong Type I and Type III interferon responses towards immunostimulatory NANPs (Figure 4). For all analytes tested, CpG-OH-displaying PB84 constructs induced higher interferon expression compared with their unmodified counterparts. Additionally, interferon production was generally, and in some cases significantly, higher in response to PB84 displaying 40 copies of CpG-OH compared to PB84 with 20 copies of CpG-OH, the same trend that was observed in the HEK-Blue TLR9 reporter cells. In contrast, when ICO42 with 0, 20, and 30 copies of CpG-OH were transfected into PBMCs, the increase in IFN response towards ICO42 displaying CpG-OHs appeared to saturate at 20 CpG-OHs. In most cases, ICO42 displaying 30 copies of CpG-OH induced similar levels of IFNs to the unmodified ICO42, and in a few cases, lower IFN expression was observed in response to ICO42 with 30 CpG-OHs compared to the unmodified NANP. To validate that this response was not due to the hook effect, a phenomenon common to immunoassays in which excessively high concentrations of the target analyte outcompetes the detection antibody for binding and results in an artificially low signal, we re-tested samples at several dilutions and observed the same trend, indicating that this response was accurately reported. As the peak of immune pathway activation and interferon production may occur at a different time than was analyzed in this study, a time course assay may provide further insight into these results and simultaneously elucidate the dynamics of NANP-induced innate immune activation as well. Lastly, because PBMCs consist of a heterogeneous population of immune cells such as B cells, monocytes, and dendritic cells that express multiple different DNA sensing innate immune pathways, these differences in response to distinct NANP geometries may be due to different levels of contribution from additional immune pathways besides TLR9.

In particular, while the primary focus of this study has been on the endosomal ssDNA-sensing TLR9 pathway, another critical nucleic acid sensing pathway that may be involved in the immune response towards DNA NANPs is the cGAS-STING pathway. Unlike TLR9, which requires specific sequence contexts for binding and activation, cGAS responds to cytosolic dsDNA in a primarily sequence-independent manner. As a result, while neither of the unmodified PB84 nor ICO42 constructs induced strong TLR9 signaling, we hypothesized that they might instead elicit a substantial cGAS-STING response. To test this, we transfected PB84, ICO42, and their respective unstructured controls into THP1-Dual reporter cells. After a 24-hour incubation, we observed that both structured NANPs strongly activated the cGAS-STING pathway (Figure S15), whereas the unstructured scaffold and staple controls induced lower levels of activation. As part of the PBMC assay design, in order to maintain a constant CpG concentration across samples, the concentration of NANPs, and therefore the concentration of cGAS ligand, was reduced proportionally. Therefore, the increase in IFN expression between PB84 displaying 20 CpG-OH and 40 CpG-OH occurred despite NANP concentration being halved between samples, suggesting that the increase in TLR9 activation was strong enough to overcome the decrease in cGAS-STING activation. However, in the case of ICO42, the interferon expression triggered by the

0 CpG-OH construct was already significant, suggesting that the primary pathway involved in the ICO42-mediated immune response might be cGAS-STING.

CONCLUDING DISCUSSION

We characterized the baseline immunostimulatory effects of wireframe DNA origami nanoparticles in reporter cell lines and found that unmodified nanostructures did not induce a substantive TLR9 response. However, when these nanostructures were functionalized with immunostimulatory CpG overhangs, changing the valency of CpGs attached to the NANP resulted in controllably modulated TLR9 activation levels, even when the total CpG concentration was kept constant. This suggested that the magnitude of TLR9 activation was dependent on not only CpG concentration, but also parameters governing the nanoscale display of CpG overhangs such as inter-CpG distance, consistent with results from a prior study that examined CpG dimers alone.[29]

To investigate the effects of multivalency and three-dimensional spatial display of CpGs, we used wireframe DNA origami NANPs to fabricate constructs with controlled numbers of attached CpG-OHs to characterize the impact of these parameters on TLR9 activation. We found that changing the 3D structure of the nanoparticle upon which CpG overhangs were displayed, for example from an icosahedron to a tetrahedron, resulted in different magnitudes of TLR9 activation, revealing that 3D spatial distribution of CpG overhangs, even with fixed inter-CpG spacing, influences TLR9 signaling. Moreover, the 3D nature of our NANPs enabled us to systematically test a variety of different parameters such as inward versus outward orientation of CpG overhangs and spatial organization of CpG dimers with both fixed and variable spacing across a wide range of NANPs with different 3D structures. These results revealed the importance of 3D structure and multivalency on TLR9 signaling.

To evaluate our designs in a physiologically relevant system that mimics the complex environment that nanoparticles might face upon intravenous injection, we tested our engineered immunostimulatory NANPs in primary immune cells and found that for certain geometries, we were able to controllably modulate downstream production of Type I and III IFNs using the preceding design parameters identified in our work. However, we also found that this method of tuning NANP immunostimulation was not directly transferrable across all NANP geometries, so further work is needed to resolve the mechanistic basis of immune activation by wireframe NANPs, in particular by identifying and further investigating the specific subsets of immune cells that are primarily responsible for driving the NANP-induced immune response.

In addition, an intriguing question is how the relative contributions of cGAS-STING and TLR9 change across different NANPs and how these differences affect downstream interferon production. As observed in Figure 4, the expression levels of IFNs incubated with ICO42 displaying 30 CpG overhangs decreased or exhibited no differences compared to unmodified ICO42, in contrast to the increase in IFN expression induced by PB84 displaying CpG-OHs. Because the bare ICO42 induced significantly higher levels of IFN production compared to bare PB84, a potential explanation for this observation is that when the concentration of ICO42 was decreased across samples to keep the CpG

concentration constant, the increase in TLR9 signaling might not have been sufficient to compensate for the loss of cGAS-STING activation in response to this particular NANP geometry. These results imply that the relative contributions of different DNA-sensing innate immune pathways differ across NANP geometries. Consequently, the method of enhancing nanoparticle immunostimulatory properties may be different depending on which pathway is more strongly engaged by a specific NANP shape. This hypothesis may be tested by further investigating the effects of NANP geometries on additional nucleic acid sensing pathways such as AIM2.

Another open question is whether our NANPs can be internalized by immune cells such as macrophages in the absence of transfection reagents. We showed in both reporter cell lines and PBMCs that NANPs that were not complexed with lipofectamine did not elicit immune pathway activation (Figure S5, S17). However, lack of immune signaling does not rule out internalization. For example, the concentration of internalized structures or their duration of internalization may not have been sufficient to induce detectable cytokine expression. Investigating this would require systematic evaluation of immune pathway activation in PBMC cell subsets and reporter cell lines, as well as examining interferon production in PBMCs over longer timescales than investigated in this study, possibly also using stabilized NANPs.[16,17,61] Investigating cellular binding and endocytosis directly with flow cytometry and confocal microscopy of fluorescently labeled NANPs to characterize NANP internalization in distinct cell types would also be highly valuable to complement this work. Indeed, understanding the endocytic pathways through which NANPs may be endocytosed by visualizing trafficking upon internalization with and without transfection reagents, or including cell-specific targeting ligands, would be of significant interest in the future. Lastly, another important question that would be interesting to explore in future work is whether wireframe DNA NANPs primarily modulate TLR9 activation levels by enhancing activation of individual TLR9 dimers or if they are capable of coordinating activation of clusters of TLR9 dimers, a question that might be resolved using super-resolution fluorescence imaging.[64–66]

While nucleic acid nanodevices have been applied to various therapeutic areas, their immunostimulatory properties have been explored to a lesser degree. Such fundamental understanding of NANP immunological properties is important to inform the design of follow-on *in vivo* studies using CpG overhangs (e.g., Zeng *et al.,* bioRxiv and Oktay *et al.*, bioRxiv), to further explore prophylactic and therapeutic potential of these nanomaterials.[67,68] By establishing a deeper understanding of the baseline immunostimulatory properties of unmodified wireframe NANPs and the relative impacts of various NANP design parameters on DNA nanoparticle-mediated tunable TLR9 activation, we can work towards enabling the design of DNA nanostructures with specific immunostimulatory profiles for targeted biological outcomes.

MATERIALS AND METHODS

Scaffold Synthesis.

The circular ssDNA scaffolds used to fold all variants of PB84 and ICO42 described in the paper were produced using a previous published method of bacterial production.[22] *E.*

coli SS320 cells (Lucigen) containing the circular phagemid comprising the target scaffold sequence and a M13cp helper plasmid, provided by Dr. Andrew Bradbury (Los Alamos National Laboratory), were grown overnight in 25mL 2 x YT broth (Sigma Aldrich, cat. code Y2377) supplemented with 100 ug/mL ampicillin (Sigma-Aldrich, cat. code A5354–10ML), 15 ug/mL chloramphenicol (Sigma-Aldrich, cat. code C0378–25G) and 5 ug/mL tetracycline (Sigma-Aldrich, cat. code T7660) in a 200mL flask shaken at 200 RPM at 37C. After 16 hours, the overnight was diluted to an OD600 of 0.05 in 2 x YT broth containing the same supplements and grown for 8 hours at 200 RPM at 37C.

Scaffold Purification.

Bacterial cultures were centrifuged at 4000 x g for 30 minutes at 4C, transferred into a clean bottle, and subjected to an identical centrifugation step. The clarified supernatant was then filtered with a 0.45 um cellulose acetate filter (Sigma-Aldrich, cat. code CLS430516–12EA), poured into a sterile 750mL bottle along with 6% w/v PEG-8000 (Sigma-Aldrich, cat. code P2139–500G) and 3% w/v NaCl (Sigma Aldrich, cat. code 7647145), and stirred continuously for 16 hours at 4C. Following PEG precipitation, phage was harvested by centrifuging the solution at 20,000 x g for 30 hour at 4C and discarding the supernatant. The phage-containing pellet was then processed using an Endofree Plasmid Giga Kit (Qiagen, cat. code 12391), with the following adjustments: a final concentration of 20 ug/mL Proteinase K (Sigma Aldrich, cat. code 3115828001) was added to Buffer P1, and the solution was incubated at 37C for 1 hour prior to addition of Buffer P2. Following Buffer P2 addition, the solution was heated to 70C for 10 minutes and allowed to cool back to room temperature before proceeding with the rest of the standard protocol. Finally, after addition of Buffer ER, 200mL of 100% ethanol was added to improve ssDNA binding. All remaining steps are left unchanged. The concentration of purified ssDNA was determined by measuring absorbance at 280nm using a Nanodrop (Thermo Scientific, cat. code 13400518), and the purity of the sample was evaluated by running it on a 1% agarose gel in 1X TAE stained with SybrSafe. A quantitative measure of sample endotoxin level was determined using Endosafe LAL cartridges (Charles River Laboratories, cat. code PTS2001F) with the Endosafe nexgen-PTS system (Charles River Laboratories, cat. code PTS150K), and Rapid Single-Test LAL vials (Charles River Laboratories, cat. code r135) were used to establish qualitatively whether sample endotoxin levels were below a pre-specified threshold. Both endotoxin assays were performed according to manufacturer protocols.

Endotoxin Purification.

In the cases when additional endotoxin purification was needed, chilled 10% v/v Triton X-114 (MilliporeSigma, cat. code 648468–50mL) was added to the sample to a final concentration of 2% v/v Triton X-114. The sample was placed on a rocker at 4C for 30 minutes, then transferred to a rocker at 37C for 5 minutes. Lastly, the sample was centrifuged at 30790x*g* for 30 minutes at 37C. The sample was then carefully removed from the centrifuge and the top layer of the phase-separated sample was gently pipetted into an endotoxin-free microcentrifuge tube. This process was repeated until sample endotoxin levels were below the desired threshold for subsequent assays.

Synthesis and Purification of DNA NANPs.

NANPs were designed using DAEDALUS, with modifications to add ssDNA overhangs being carried out in Tiamat or UCSF Chimera. Briefly, to design inward- or outward-facing overhangs, the locations of nick positions were shifted by the required number of bases to ensure that the 3' ends of staples would be pointing perpendicularly inward or outward with respect to the center of the nanostructure. No additional nicks were created and all new nick positions were located such that at least 8 bases separated the nick position from the location of the nearest crossover. The modified NANP designs were exported into Excel, and the staples chosen to be functionalized with ssDNA overhangs were extended by concatenating the sequence of the overhang to the 3' end of the existing staple sequence (Supplementary Table 2). To fold NANPs, a circular exact size bacterially produced ssDNA scaffold was mixed with a 5X excess of ssDNA staples, 1X TAE, 12mM $MgCl_2$, and nuclease-free water, and folded through a 13 hour thermal annealing process in which the temperature was gradually ramped down from 95C to 25C as described in previous literature.[9] To remove the excess staples and buffer exchange into sterile PBS, nanostructures were pipetted into Amicon Ultra 100kDa MWCO centrifugal filters (Sigma-Aldrich, cat. code UFC810024) and spun at 1000x*g* for 30 minutes at room temperature for up to 5 rounds. In between each round, the flow-through was discarded and additional PBS was added. Staples were purchased through Integrated DNA Technologies (IDT) or synthesized in-house using a Dr. Oligo synthesizer following the recommended protocol and purified using a size exclusion column with a Waters HPLC. Phosphoramidites for in-house synthesis of the phosphorothioated CpG overhang-containing staples (Supplementary Table 2) were ordered from Glen Research.

Gel Shift Assay, Dynamic Light Scattering, Fluorimetry.

Agarose gel electrophoresis was used to analyze degree of NANP folding. 1.5% low melt agarose (IBI Scientific, cat. code IB70057) was dissolved in buffer containing 1X TAE (Corning, cat. code 46–010-cm) and 12 mM $MgCl_2$ (Sigma Aldrich, cat. code M2670) and slowly heated to boiling, then cooled back to room temperature. SybrSafe was mixed into the gel according to manufacturer protocols and the gel was allowed to set for at least 45 minutes at room temperature or 4C prior to gel electrophoresis. 100ng of DNA NANP sample was mixed with gel loading buffer (final concentration 1X) with water to make up the necessary volume. The gel was placed in a chamber containing pre-chilled gel running buffer consisting of 1X TAE and 12mM $MgCl_2$, and once the samples were loaded, the gel was run at 85V for 120 minutes at 4C. Images were captured using a Typhoon FLA 7000 (GE Healthcare). DLS was used for validation of NANP monodispersity: samples were diluted to 50nM in PBS, and 50uL of each sample was loaded into a plastic cuvette to be evaluated on a ZetaSizer Nano ZSP (Malvern Analytical). Samples were analyzed in triplicate using single angle scattering. Quantification of CpG copy number on NANPs was measured using a Tecan Spark. A Cy5-conjugated ssDNA oligo purchased from IDT was hybridized to folded NANPs via a 4 hour thermal annealing ramp during which the sample temperature was decreased incrementally from 37C to 25C. Fluorescently labeled NANPs were purified using the spin purification method described above and concentration was determined using UV-Vis measurements taken on a Nanodrop with absorbances set to 260nm and 647nm. A fluorescent calibration curve was produced using serial dilutions of

the free CpG overhang hybridized to the Cy5-conjugated ssDNA oligo and measured with the Tecan Spark to produce a regression line with which the coverage of CpGs on each NANP variant was determined.

Reporter Cell Assays.

HEK-Blue TLR9 cells (Invivogen, cat. code hkb-htlr9) and THP1-Dual cells (Invivogen, cat. code thpd-nfis) were cultured according to manufacturer protocols. One day prior to cell assays, TLR9 cells were detached from the flask, centrifuged at 250x*g* for 5 minutes at room temperature and resuspended in fresh growth medium, consisting of Dulbecco's Modified Eagle Medium with 4.5 g/L glucose (Sigma-Aldrich, cat. code D6546–6X500ML), 10% heat-inactivated FBS (Fisher Scientific, cat. code SH3007002HI), 100 U/mL penicillin, 100 ug/mL streptomycin (Life Technologies, cat. code 15140148), 100 ug/mL Normocin (Invivogen, cat. code ant-nr) and 2mM L-glutamine (Fisher Scientific, cat. code SH3003401). Cells were counted using a Cellometer Auto 2000 (Nexcelom) and 80,000 cells were seeded in 160uL media into a flat-bottom 96-well plate. Cells were allowed to adhere for 24 hours prior to removal of growth medium from each well and subsequent addition of 160uL of prewarmed HEK-Blue Detection Medium (Invivogen, cat. code hb-det). To prepare NANP samples, 1uM NANP stock was mixed with Lipofectamine 2000 at a ratio of 4 uL:1 uL and incubated for 30 minutes at room temperature. OptiMEM was then added to dilute NANP samples to a working concentration of 50nM. 40uL of NANP sample was added to each well, with each sample being tested in triplicate, and cells were incubated at 37C and 5% CO_2 for 20–24 hours. TLR9 activation levels were quantified by reading the absorbance of the 96-well plate at 620–655nm using a spectrophotometer and normalized to a PBS negative control. For cGAS-STING assays, THP1-Dual reporter cells were centrifuged at 250x*g* for 5 minutes at room temperature and resuspended in fresh test medium, consisting of RPMI 1640 (Life Technologies, cat. code 11875093), 25mM HEPES (Sigma Aldrich, cat. code 54457–250g-f), 10% heat-inactivated FBS, 100 U/mL penicillin, and 100 ug/mL streptomycin. 100,000 cells in 160uL media were seeded into a flat-bottom 96-well plate and 40uL of NANP sample was added to each well, with each sample being tested in triplicate. Cells were incubated at 37C and 5% CO_2 for 20–24 hours, after which 20uL of cell supernatant was carefully transferred into an opaque white 96-well plate. The plate was loaded into a Tecan Infinite 200 Pro with an injector module and the injector was set to the following parameters: 50uL injection per well, end-point measurement, 4 second delay, 0.1 second reading time. The injector was primed with QUANTI-Luc assay solution (Invivogen, cat. code rep-qlc1), and the measurement was taken. Positive controls for TLR9 and cGAS-STING assays were not complexed with lipofectamine prior to incubation with PBMCs.

PBMC Isolation, Stimulation, and Multiplex ELISA.

Research donor blood was obtained from anonymous healthy donor volunteers under the IRB approved NCI-at-Frederick Protocol OH9-C-N046 and the MIT IRB approved exemption E-3359. PBMCs were isolated from three separate human donor buffy coats following the NCL protocol ITA-10 and tested following protocol ITA-27.[69] Briefly, blood was mixed at a 1:1 ratio with fresh PBS and gently layered onto Ficoll-Paque (Fisher Scientific, cat. code 45001751) at a ratio of 3 mL Ficoll-Paque to 4mL diluted blood

in a 50mL Falcon tube. Tubes were centrifuged at 900x*g* for 30 minutes with minimum acceleration and with the brakes off, after which the PBMC layer was gently pipetted into a new 50mL tube. PBMCs were washed three times with HBSS (Life Technologies, cat. code 24020117) and resuspended in complete RPMI, which consisted of RPMI 1640, 10% heat-inactivated FBS, 100U/mL penicillin and 100 ug/mL streptomycin. Cells were counted using a Cellometer Auto 2000 and 1.25×10^6 cells in 160uL media were seeded into a flat-bottom 96-well plate. NANP samples were complexed with Lipofectamine 2000 (Life Technologies, cat. code 11668027) at a ratio of 4:1 and incubated at room temperature for 30 minutes, after which OptiMEM (Life Technologies, cat. code 31985062) was added to dilute the NANPs to the correct working concentration. 40uL of the lipofectamine-complexed NANP sample was added to each well, with each sample being tested in triplicate, and cells were incubated at 37C and 5% CO_2 for 20–24 hours. 150uL of cell supernatant was carefully transferred into a new 96-well plate, and the plate was flash frozen and stored at −80C. Supernatant was then shipped on dry ice to Quansys Biosciences, which analyzed production of IFNα, IFNβ, IFNω, and IFNλ using multiplexed ELISA.

Supplementary Material

Refer to Web version on PubMed Central for supplementary material.

ACKNOWLEDGEMENTS:

We are grateful to Dr. Xiao Wang for synthesizing phosphorothioated oligonucleotide staples, to Grant Knappe for synthesizing Cy5 staples, and to Dr. Eike-Christian Wamhoff for feedback on this manuscript. R.R.D. and M.B. were supported by ONR N00014-17-1-2609, NIH R01-MH112694, Fast Grant AGMT EFF 4/15/20, ISN W911NF-13-D-0001, NIH R21EB026008, Supplement R21-EB026008-S1, ONR N00014-21-1-4013, NIH R01-AI162307, and NIH TG BTP T32-GM008334. R.F. was supported by NIH R01-MH112694-05 and NSF PoLS2 PHY-1707999. A.R. was supported by NIH R01-AI162307-02 and NSF GRFP 2020294332. E.C. and M.A.D. were supported in part by federal funds from the National Cancer Institute, National Institutes of Health, under contract 75N91019D00024. The content of this publication does not necessarily reflect the views or policies of the Department of Health and Human Services, nor does mention of trade names, commercial products, or organizations imply endorsement by the U.S. Government. This work made use of the CEHS Facilities core, funded by the NIEHS Center Core grant P30-ES002109.

REFERENCES

(1). Jun H; Wang X; Parsons MF; Bricker WP; John T; Li S; Jackson S; Chiu W; Bathe M. Rapid Prototyping of Arbitrary 2D and 3D Wireframe DNA Origami. Nucleic Acids Res 2021, 49 (18), 10265–10274. 10.1093/nar/gkab762. [PubMed: 34508356]

(2). Pettersen EF; Goddard TD; Huang CC; Couch GS; Greenblatt DM; Meng EC; Ferrin TE UCSF Chimera-- A Visualization System for Exploratory Research and Analysis. J Comput Chem 2004, 25 (13), 1605–1612. 10.1002/jcc.20084. [PubMed: 15264254]

(3). Benson E; Mohammed A; Bosco A; Teixeira AI; Orponen P; Högberg B. Computer-Aided Production of Scaffolded DNA Nanostructures from Flat Sheet Meshes. Angewandte Chemie International Edition 2016, 55 (31), 8869–8872. 10.1002/anie.201602446. [PubMed: 27304204]

(4). Jun H; Shepherd TR; Zhang K; Bricker WP; Li S; Chiu W; Bathe M. Automated Sequence Design of 3D Polyhedral Wireframe DNA Origami with Honeycomb Edges. ACS Nano 2019, acsnano.8b08671. 10.1021/acsnano.8b08671.

(5). Benson E; Mohammed A; Gardell J; Masich S; Czeizler E; Orponen P; Högberg B. DNA Rendering of Polyhedral Meshes at the Nanoscale. Nature 2015, 523 (7561), 441–444. 10.1038/nature14586. [PubMed: 26201596]

(6). Dietz H; Douglas SM; Shih WM Folding DNA into Twisted and Curved Nanoscale Shapes. Science (1979) 2009, 325 (5941), 725–730. 10.1126/science.1174251.

(7). Castro CE; Kilchherr F; Kim D-N; Shiao EL; Wauer T; Wortmann P; Bathe M; Dietz H. A Primer to Scaffolded DNA Origami. Nat Methods 2011, 8 (3), 221–229. 10.1038/nmeth.1570. [PubMed: 21358626]

(8). Douglas SM; Marblestone AH; Teerapittayanon S; Vazquez A; Church GM; Shih WM Rapid Prototyping of 3D DNA-Origami Shapes with CaDNAno. Nucleic Acids Res 2009, 37 (15), 5001–5006. 10.1093/nar/gkp436. [PubMed: 19531737]

(9). Veneziano R; Ratanalert S; Zhang K; Zhang F; Yan H; Chiu W; Bathe M. Designer Nanoscale DNA Assemblies Programmed from the Top Down. Science (1979) 2016, 352 (6293), 1534–1534. 10.1126/science.aaf4388.

(10). Krishnan Y; Bathe M. Designer Nucleic Acids to Probe and Program the Cell. Trends Cell Biol 2012, 22 (12), 624–633. 10.1016/j.tcb.2012.10.001. [PubMed: 23140833]

(11). Veneziano R; Moyer TJ; Stone MB; Wamhoff E-C; Read BJ; Mukherjee S; Shepherd TR; Das J; Schief WR; Irvine DJ; Bathe M. Role of Nanoscale Antigen Organization on B-Cell Activation Probed Using DNA Origami. Nat Nanotechnol 2020, 15 (8), 716–723. 10.1038/s41565-020-0719-0. [PubMed: 32601450]

(12). Lee H; Lytton-Jean AKR; Chen Y; Love KT; Park AI; Karagiannis ED; Sehgal A; Querbes W; Zurenko CS; Jayaraman M; Peng CG; Charisse K; Borodovsky A; Manoharan M; Donahoe JS; Truelove J; Nahrendorf M; Langer R; Anderson DG Molecularly Self-Assembled Nucleic Acid Nanoparticles for Targeted in Vivo SiRNA Delivery. Nat Nanotechnol 2012, 7 (6), 389–393. 10.1038/nnano.2012.73. [PubMed: 22659608]

(13). Douglas SM; Bachelet I; Church GM A Logic-Gated Nanorobot for Targeted Transport of Molecular Payloads. Science (1979) 2012, 335 (6070), 831–834. 10.1126/science.1214081.

(14). Hoshyar N; Gray S; Han H; Bao G. The Effect of Nanoparticle Size on in Vivo Pharmacokinetics and Cellular Interaction. Nanomedicine 2016, 11 (6), 673–692. 10.2217/nnm.16.5. [PubMed: 27003448]

(15). Perrault SD; Walkey C; Jennings T; Fischer HC; Chan WCW Mediating Tumor Targeting Efficiency of Nanoparticles Through Design. Nano Lett 2009, 9 (5), 1909–1915. 10.1021/nl900031y. [PubMed: 19344179]

(16). Zhang Y-N; Lazarovits J; Poon W; Ouyang B; Nguyen LNM; Kingston BR; Chan WCW Nanoparticle Size Influences Antigen Retention and Presentation in Lymph Node Follicles for Humoral Immunity. Nano Lett 2019, 19 (10), 7226–7235. 10.1021/acs.nanolett.9b02834. [PubMed: 31508968]

(17). Wamhoff E-C; Romanov A; Huang H; Read BJ; Ginsburg E; Knappe GA; Kim HM; Farrell NP; Irvine DJ; Bathe M. Controlling Nuclease Degradation of Wireframe DNA Origami with Minor Groove Binders. ACS Nano 2022. 10.1021/acsnano.1c11575.

(18). Ponnuswamy N; Bastings MMC; Nathwani B; Ryu JH; Chou LYT; Vinther M; Li WA; Anastassacos FM; Mooney DJ; Shih WM Oligolysine-Based Coating Protects DNA Nanostructures from Low-Salt Denaturation and Nuclease Degradation. Nat Commun 2017, 8 (1), 15654. 10.1038/ncomms15654. [PubMed: 28561045]

(19). Rothemund PWK Folding DNA to Create Nanoscale Shapes and Patterns. Nature 2006, 440 (7082), 297–302. 10.1038/nature04586. [PubMed: 16541064]

(20). Praetorius F; Kick B; Behler KL; Honemann MN; Weuster-Botz D; Dietz H. Biotechnological Mass Production of DNA Origami. Nature 2017, 552 (7683), 84–87. 10.1038/nature24650. [PubMed: 29219963]

(21). Engelhardt FAS; Praetorius F; Wachauf CH; Brüggenthies G; Kohler F; Kick B; Kadletz KL; Pham PN; Behler KL; Gerling T; Dietz H. Custom-Size, Functional, and Durable DNA Origami with Design-Specific Scaffolds. ACS Nano 2019, 13 (5), 5015–5027. 10.1021/acsnano.9b01025. [PubMed: 30990672]

(22). Shepherd TR; Du RR; Huang H; Wamhoff E-C; Bathe M. Bioproduction of Pure, Kilobase-Scale Single-Stranded DNA. Sci Rep 2019, 9 (1), 6121. 10.1038/s41598-019-42665-1. [PubMed: 30992517]

(23). Knappe GA; Wamhoff E-C; Read BJ; Irvine DJ; Bathe M. In Situ Covalent Functionalization of DNA Origami Virus-like Particles. ACS Nano 2021, 15 (9), 14316–14322. 10.1021/acsnano.1c03158. [PubMed: 34490781]

(24). Liu X; Xu Y; Yu T; Clifford C; Liu Y; Yan H; Chang Y. A DNA Nanostructure Platform for Directed Assembly of Synthetic Vaccines. Nano Lett 2012, 12 (8), 4254–4259. 10.1021/nl301877k. [PubMed: 22746330]

(25). Irvine DJ; Hanson MC; Rakhra K; Tokatlian T. Synthetic Nanoparticles for Vaccines and Immunotherapy. Chem Rev 2015, 115 (19), 11109–11146. 10.1021/acs.chemrev.5b00109. [PubMed: 26154342]

(26). Surana S; Shenoy AR; Krishnan Y. Designing DNA Nanodevices for Compatibility with the Immune System of Higher Organisms. Nat Nanotechnol 2015, 10 (9), 741–747. 10.1038/nnano.2015.180. [PubMed: 26329110]

(27). Hong E; Halman J; Shah A; Cedrone E; Truong N; Afonin K; Dobrovolskaia M. Toll-Like Receptor-Mediated Recognition of Nucleic Acid Nanoparticles (NANPs) in Human Primary Blood Cells. Molecules 2019, 24 (6), 1094. 10.3390/molecules24061094. [PubMed: 30897721]

(28). Schüller VJ; Heidegger S; Sandholzer N; Nickels PC; Suhartha NA; Endres S; Bourquin C; Liedl T. Cellular Immunostimulation by CpG-Sequence-Coated DNA Origami Structures. ACS Nano 2011, 5 (12), 9696–9702. 10.1021/nn203161y. [PubMed: 22092186]

(29). Comberlato A; Koga MM; Nüssing S; Parish IA; Bastings MMC Spatially Controlled Activation of Toll-like Receptor 9 with DNA-Based Nanomaterials. Nano Lett 2022, acs.nanolett.2c00275. 10.1021/acs.nanolett.2c00275.

(30). Li J; Pei H; Zhu B; Liang L; Wei M; He Y; Chen N; Li D; Huang Q; Fan C. Self-Assembled Multivalent DNA Nanostructures for Noninvasive Intracellular Delivery of Immunostimulatory CpG Oligonucleotides. ACS Nano 2011, 5 (11), 8783–8789. 10.1021/nn202774x. [PubMed: 21988181]

(31). Hong E; Halman JR; Shah AB; Khisamutdinov EF; Dobrovolskaia MA; Afonin KA Structure and Composition Define Immunorecognition of Nucleic Acid Nanoparticles. Nano Lett 2018, 18 (7), 4309–4321. 10.1021/acs.nanolett.8b01283. [PubMed: 29894623]

(32). Guo S; Li H; Ma M; Fu J; Dong Y; Guo P. Size, Shape, and Sequence-Dependent Immunogenicity of RNA Nanoparticles. Mol Ther Nucleic Acids 2017, 9, 399–408. 10.1016/j.omtn.2017.10.010. [PubMed: 29246318]

(33). Lucas CR; Halley PD; Chowdury AA; Harrington BK; Beaver L; Lapalombella R; Johnson AJ; Hertlein EK; Phelps MA; Byrd JC; Castro CE DNA Origami Nanostructures Elicit Dose-Dependent Immunogenicity and Are Nontoxic up to High Doses In Vivo. Small 2022, 2108063. 10.1002/smll.202108063.

(34). Liu S; Jiang Q; Zhao X; Zhao R; Wang Y; Wang Y; Liu J; Shang Y; Zhao S; Wu T; Zhang Y; Nie G; Ding B. A DNA Nanodevice-Based Vaccine for Cancer Immunotherapy. Nat Mater 2021, 20 (3), 421–430. 10.1038/s41563-020-0793-6. [PubMed: 32895504]

(35). Schlee M; Hartmann G. Discriminating Self from Non-Self in Nucleic Acid Sensing. Nat Rev Immunol 2016, 16 (9), 566–580. 10.1038/nri.2016.78. [PubMed: 27455396]

(36). Paludan SR Activation and Regulation of DNA-Driven Immune Responses. Microbiology and Molecular Biology Reviews 2015, 79 (2), 225–241. 10.1128/MMBR.00061-14. [PubMed: 25926682]

(37). Paludan SR; Bowie AG Immune Sensing of DNA. Immunity 2013, 38 (5), 870–880. 10.1016/j.immuni.2013.05.004. [PubMed: 23706668]

(38). Wu J; Chen ZJ Innate Immune Sensing and Signaling of Cytosolic Nucleic Acids. Annu Rev Immunol 2014, 32 (1), 461–488. 10.1146/annurev-immunol032713-120156. [PubMed: 24655297]

(39). Kawai T; Akira S. The Role of Pattern-Recognition Receptors in Innate Immunity: Update on Toll-like Receptors. Nat Immunol 2010, 11 (5), 373–384. 10.1038/ni.1863. [PubMed: 20404851]

(40). Kawasaki T; Kawai T. Toll-Like Receptor Signaling Pathways. Front Immunol 2014, 5. 10.3389/fimmu.2014.00461.

(41). Krieg AM; Yi A-K; Matson S; Waldschmidt TJ; Bishop GA; Teasdale R; Koretzky GA; Klinman DM CpG Motifs in Bacterial DNA Trigger Direct B-Cell Activation. Nature 1995, 374 (6522), 546–549. 10.1038/374546a0. [PubMed: 7700380]

(42). Cervantes JL; Weinerman B; Basole C; Salazar JC TLR8: The Forgotten Relative Revindicated. Cell Mol Immunol 2012, 9 (6), 434–438. 10.1038/cmi.2012.38. [PubMed: 23085951]

(43). Majer O; Liu B; Barton GM Nucleic Acid-Sensing TLRs: Trafficking and Regulation. Curr Opin Immunol 2017, 44, 26–33. 10.1016/j.coi.2016.10.003. [PubMed: 27907816]

(44). Latz E; Verma A; Visintin A; Gong M; Sirois CM; Klein DCG; Monks BG; McKnight CJ; Lamphier MS; Duprex WP; Espevik T; Golenbock DT Ligand-Induced Conformational Changes Allosterically Activate Toll-like Receptor 9. Nat Immunol 2007, 8 (7), 772–779. 10.1038/ni1479. [PubMed: 17572678]

(45). Ohto U; Ishida H; Shibata T; Sato R; Miyake K; Shimizu T. Toll-like Receptor 9 Contains Two DNA Binding Sites That Function Cooperatively to Promote Receptor Dimerization and Activation. Immunity 2018, 48 (4), 649–658.e4. 10.1016/j.immuni.2018.03.013. [PubMed: 29625894]

(46). Deguine J; Barton GM MyD88: A Central Player in Innate Immune Signaling. F1000Prime Rep 2014, 6. 10.12703/P6-97.

(47). Marongiu L; Gornati L; Artuso I; Zanoni I; Granucci F. Below the Surface: The Inner Lives of TLR4 and TLR9. J Leukoc Biol 2019, 106 (1), 147–160. 10.1002/JLB.3MIR1218-483RR. [PubMed: 30900780]

(48). Bonham KS; Orzalli MH; Hayashi K; Wolf AI; Glanemann C; Weninger W; Iwasaki A; Knipe DM; Kagan JC A Promiscuous Lipid-Binding Protein Diversifies the Subcellular Sites of Toll-like Receptor Signal Transduction. Cell 2014, 156 (4), 705–716. 10.1016/j.cell.2014.01.019. [PubMed: 24529375]

(49). Krieg AM Toll-like Receptor 9 (TLR9) Agonists in the Treatment of Cancer. Oncogene 2008, 27 (2), 161–167. 10.1038/sj.onc.1210911. [PubMed: 18176597]

(50). Chen HC; Sun B; Tran KK; Shen H. Effects of Particle Size on Toll-like Receptor 9-Mediated Cytokine Profiles. Biomaterials 2011, 32 (6), 1731–1737. 10.1016/j.biomaterials.2010.10.059. [PubMed: 21126760]

(51). Luchner M; Reinke S; Milicic A. TLR Agonists as Vaccine Adjuvants Targeting Cancer and Infectious Diseases. Pharmaceutics 2021, 13 (2), 142. 10.3390/pharmaceutics13020142. [PubMed: 33499143]

(52). Pohar J; Kužnik Krajnik A; Jerala R; Benčina M. Minimal Sequence Requirements for Oligodeoxyribonucleotides Activating Human TLR9. The Journal of Immunology 2015, 194 (8), 3901–3908. 10.4049/jimmunol.1402755. [PubMed: 25780037]

(53). Vollmer J; Weeratna R; Payette P; Jurk M; Schetter C; Laucht M; Wader T; Tluk S; Liu M; Davis HL; Krieg AM Characterization of Three CpG Oligodeoxynucleotide Classes with Distinct Immunostimulatory Activities. Eur J Immunol 2004, 34 (1), 251–262. 10.1002/eji.200324032. [PubMed: 14971051]

(54). Yang G; Koo JE; Lee HE; Shin SW; Um SH; Lee JY Immunostimulatory Activity of Y-Shaped DNA Nanostructures Mediated through the Activation of TLR9. Biomedicine & Pharmacotherapy 2019, 112, 108657. 10.1016/j.biopha.2019.108657.

(55). Leleux JA; Pradhan P; Roy K. Biophysical Attributes of CpG Presentation Control TLR9 Signaling to Differentially Polarize Systemic Immune Responses. Cell Rep 2017, 18 (3), 700–710. 10.1016/j.celrep.2016.12.073. [PubMed: 28099848]

(56). Jin J-O; Park H; Zhang W; de Vries JW; Gruszka A; Lee MW; Ahn D-R; Herrmann A; Kwak M. Modular Delivery of CpG-Incorporated Lipid-DNA Nanoparticles for Spleen DC Activation. Biomaterials 2017, 115, 81–89. 10.1016/j.biomaterials.2016.11.020. [PubMed: 27886556]

(57). Cha BG; Jeong JH; Kim J. Extra-Large Pore Mesoporous Silica Nanoparticles Enabling Co-Delivery of High Amounts of Protein Antigen and Toll-like Receptor 9 Agonist for Enhanced Cancer Vaccine Efficacy. ACS Cent Sci 2018, 4 (4), 484–492. 10.1021/acscentsci.8b00035. [PubMed: 29721531]

(58). Tsai C-Y; Lu S-L; Hu C-W; Yeh C-S; Lee G-B; Lei H-Y Size-Dependent Attenuation of TLR9 Signaling by Gold Nanoparticles in Macrophages. The Journal of Immunology 2012, 188 (1), 68–76. 10.4049/jimmunol.1100344. [PubMed: 22156340]

(59). Lee K; Huang ZN; Mirkin CA; Odom TW Endosomal Organization of CpG Constructs Correlates with Enhanced Immune Activation. Nano Lett 2020, 20 (8), 6170–6175. 10.1021/acs.nanolett.0c02536. [PubMed: 32787186]

(60). Yue J; Pallares RM; Cole LE; Coughlin EE; Mirkin CA; Lee A; Odom TW Smaller CpG-Conjugated Gold Nanoconstructs Achieve Higher Targeting Specificity of Immune Activation. ACS Appl Mater Interfaces 2018, 10 (26), 21920–21926. 10.1021/acsami.8b06633. [PubMed: 29873227]

(61). Bauer S; Kirschning CJ; Häcker H; Redecke V; Hausmann S; Akira S; Wagner H; Lipford GB Human TLR9 Confers Responsiveness to Bacterial DNA via Species-Specific CpG Motif Recognition. Proceedings of the National Academy of Sciences 2001, 98 (16), 9237–9242. 10.1073/pnas.161293498.

(62). Motshwene PG; Moncrieffe MC; Grossmann JG; Kao C; Ayaluru M; Sandercock AM; Robinson C. v.; Latz E; Gay NJ. An Oligomeric Signaling Platform Formed by the Toll-like Receptor Signal Transducers MyD88 and IRAK-4. Journal of Biological Chemistry 2009, 284 (37), 25404–25411. 10.1074/jbc.M109.022392. [PubMed: 19592493]

(63). Leonard JN; Ghirlando R; Askins J; Bell JK; Margulies DH; Davies DR; Segal DM The TLR3 Signaling Complex Forms by Cooperative Receptor Dimerization. Proceedings of the National Academy of Sciences 2008, 105 (1), 258–263. 10.1073/pnas.0710779105.

(64). Latz E; Schoenemeyer A; Visintin A; Fitzgerald KA; Monks BG; Knetter CF; Lien E; Nilsen NJ; Espevik T; Golenbock DT TLR9 Signals after Translocating from the ER to CpG DNA in the Lysosome. Nat Immunol 2004, 5 (2), 190–198. 10.1038/ni1028. [PubMed: 14716310]

(65). Guo S-M; Veneziano R; Gordonov S; Li L; Danielson E; Perez de Arce K; Park D; Kulesa AB; Wamhoff E-C; Blainey PC; Boyden ES; Cottrell JR; Bathe M. Multiplexed and High-Throughput Neuronal Fluorescence Imaging with Diffusible Probes. Nat Commun 2019, 10 (1), 4377. 10.1038/s41467-019-12372-6. [PubMed: 31558769]

(66). Schueder F; Lara-Gutiérrez J; Beliveau BJ; Saka SK; Sasaki HM; Woehrstein JB; Strauss MT; Grabmayr H; Yin P; Jungmann R. Multiplexed 3D Super-Resolution Imaging of Whole Cells Using Spinning Disk Confocal Microscopy and DNA-PAINT. Nat Commun 2017, 8 (1), 2090. 10.1038/s41467-017-02028-8. [PubMed: 29233999]

(67). Zeng YC; Young OJ; Wintersinger CM; Anastassacos FM; MacDonald JI; Isinelli G; Dellacherie MO; Sobral M; Bai H; Graveline AR; Vernet A; Sanchez M; Mulligan K; Choi Y; Ferrante TC; Keskin DB; Fell GG; Neuberg D; Wu CJ; Mooney DJ; Kwon IC; Ryu JH; Shih WM Optimizing CpG Spatial Distribution with DNA Origami for Th1-Polarized Therapeutic Vaccination. bioRxiv 2022, 2022.06.08.495340. 10.1101/2022.06.08.495340.

(68). Oktay E; Alem F; Hernandez K; Narayanan A; Veneziano R. DNA Origami Presenting the Receptor Binding Domain of SARS-CoV-2 Elicit Robust Protective Immune Response. bioRxiv 2022, 2022.08.02.502186. 10.1101/2022.08.02.502186.

(69). Dobrovolskaia MA; Afonin KA Use of Human Peripheral Blood Mononuclear Cells to Define Immunological Properties of Nucleic Acid Nanoparticles. Nat Protoc 2020, 15 (11), 3678–3698. 10.1038/s41596-020-0393-6. [PubMed: 33097923]

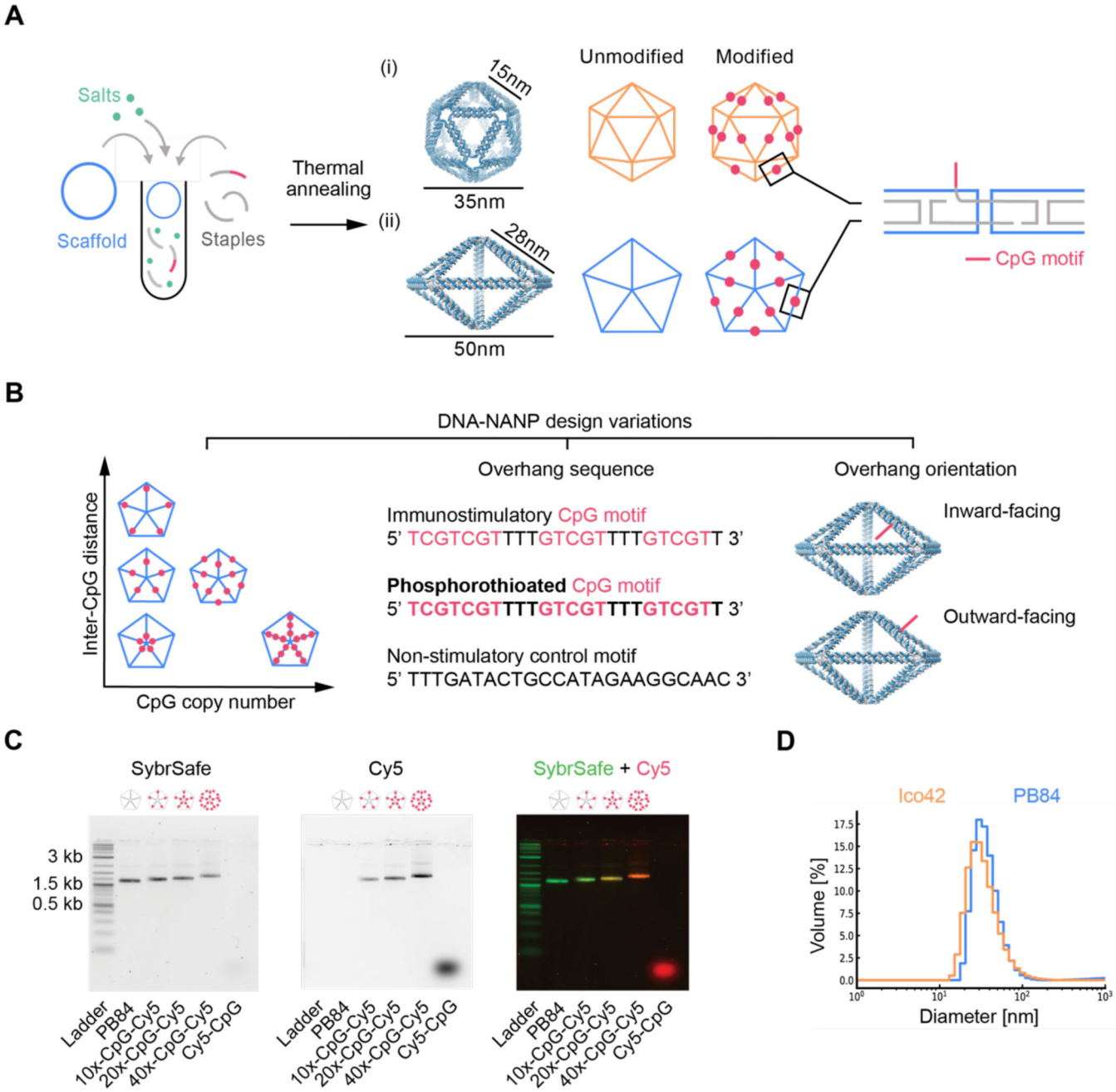

Figure 1. NANP design and characterization.

(A) DNA NANPs of varying sizes and geometries were fabricated using staples that were either unmodified or extended with ssDNA overhangs containing CpG motifs. The location and copy number of these CpG overhangs can be precisely controlled. Here we focused on two structures: (i) an icosahedron displaying up to 30 CpG overhangs, and a (ii) pentagonal bipyramid displaying up to 40 CpG overhangs. Red circles denote locations along NANP edges where CpG overhangs are displayed. (B) Design variations were used to explore the effects of CpG overhang copy number, inter-CpG distance, orientation, sequence, and oligonucleotide composition. (C) A fluorescent agarose gel shift assay was

used to analyze the quality of NANP folding after spin column purification. Pentagonal bipyramids displaying 0, 10, 20, or 40 ssDNA overhangs were hybridized to complementary Cy5-modified oligos. The gel image of the SybrSafe channel shows gel shifts corresponding to the increasing molecular weight of each construct, while the gel image taken in the Cy5 channel exhibits an increase in band intensity due to the successive increase in Cy5-CpG copy number on each NANP. Similarly, the increase in Cy5-CpG valency is demonstrated by the shift from SybrSafe green to Cy5 red in successive lanes in the SybrSafe/Cy5 overlay gel image. Gel shift assays for icosahedral constructs are shown in Figure S1. (D) Dynamic light scattering (DLS) was used to evaluate NANP hydrodynamic diameter and polydispersity. Representative DLS measurements of an unmodified pentagonal bipyramid and an icosahedron are shown; measurements for all other NANP constructs tested are shown in Figure S2.

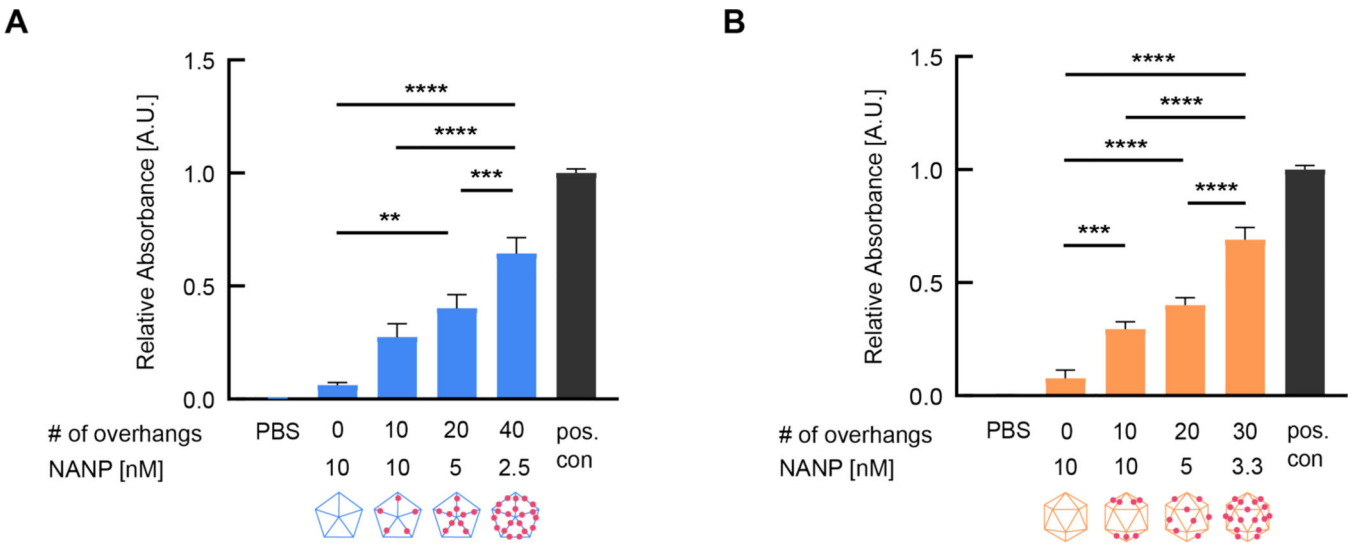

Figure 2. Magnitude of TLR9 activation can be modulated by varying copy number of CpG overhangs (CpG-OHs) displayed on NANPs.

The strength of TLR9 activation corresponds to the valency of CpG-OHs for both (A) PB84 and (B) Ico42 NANPs. The overall concentration of CpG-OHs was held constant across samples by decreasing NANP concentrations correspondingly. For all assays, baseline absorbances were determined from the PBS control and subtracted from experimental samples. Absorbances were then normalized to the ODN2006 positive control (pos. con). Data show the average absorbance of samples in triplicate with standard error, where n = 3 biologically independent assays performed on separate days. P values are from a one-sided analysis of variance (ANOVA) with a post-hoc Tukey test to correct for multiple comparisons (*: $P \leq 0.05$; **: $P \leq 0.01$, ***: $P \leq 0.001$, ****: $P \leq 0.0001$). All unlabeled pair-wise comparisons are not significant.

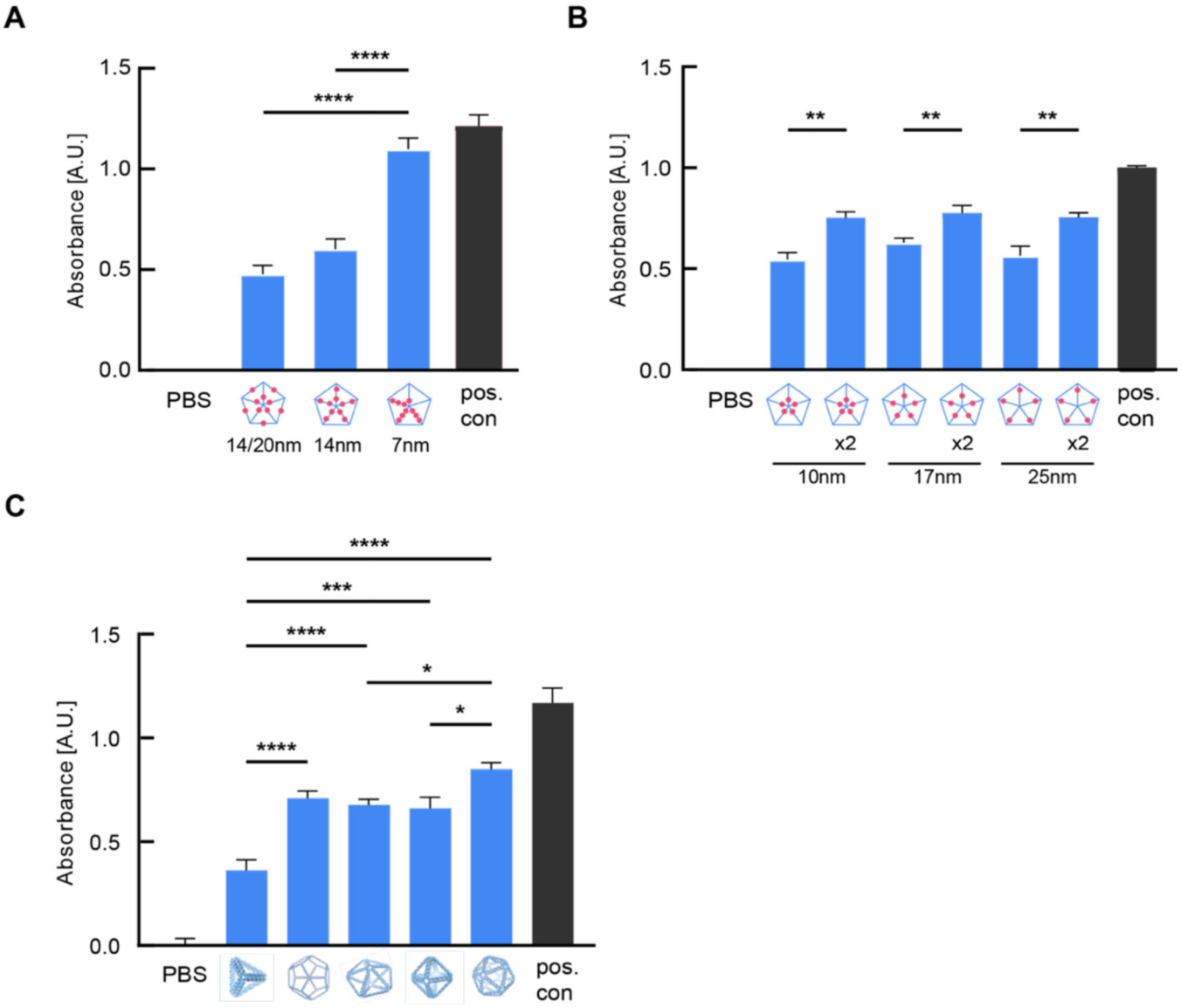

Figure 3. Magnitude of TLR9 activation is dependent on inter-CpG distance, CpG-OH nanoscale organization, and NANP geometry.

(A) TLR9 activation measured in response to stimulation with PB84 displaying 10 CpG-OHs at varying inter-CpG distances shows that the strongest activation is induced by the construct in which adjacent CpGs were displayed 7nm apart. (B) PB84 constructs were folded with either one or both sides of the NANP displaying 5 CpG-OHs. Total CpG-OH concentration was kept constant across all samples. TLR9 activation is significantly stronger for constructs in which both sides of PB84 were modified with CpG-OHs compared to their single-sided counterparts. (C) Significant differences in the magnitude of TLR9 activation were observed in response to stimulation by CpG overhangs displayed on different NANP geometries folded from the same phPB84 scaffold: a tetrahedron (Tet210), octahedron (Oct105), PB84, ICO42, and a dodecahedron (Dod42). Total CpG-OH concentration was kept constant across all samples. Baseline absorbances were determined from the PBS control and subtracted from experimental samples. Absorbances were then normalized to

the ODN2006 positive control (pos. con). Data show the average absorbance of samples in triplicate with standard error, where n = 3 biologically independent assays. P values are from a one-sided analysis of variance (ANOVA) with a post-hoc Tukey test to correct for multiple comparisons (*: $P \leq 0.05$; **: $P \leq 0.01$, ***: $P \leq 0.001$, ****: $P \leq 0.0001$). All unlabeled pair-wise comparisons are not significant.

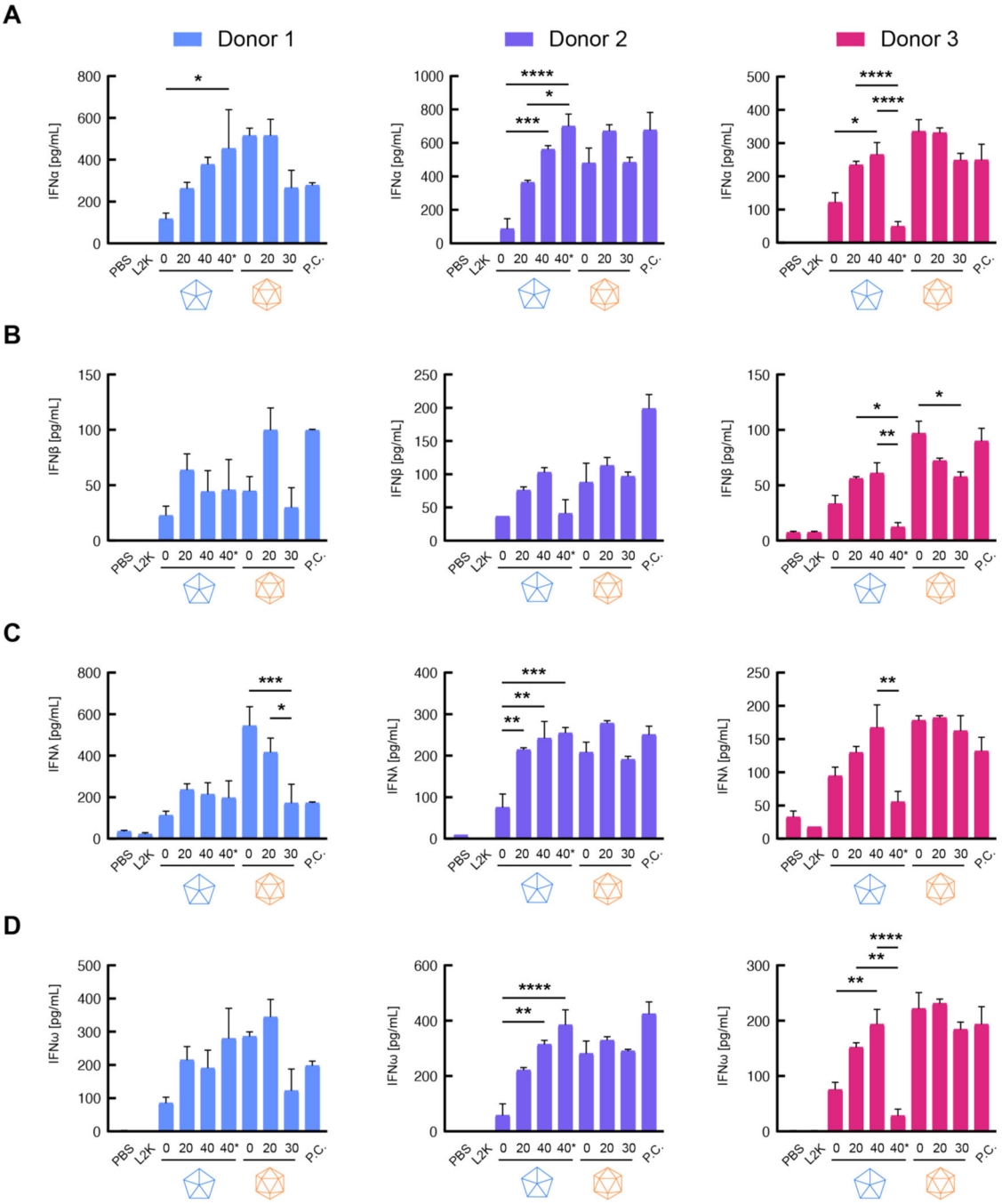

Figure 4. Interferon expression levels in PBMCs can be modulated by engineered immunostimulatory NANPs.

Elevated levels of (A) IFNα, (B) IFNβ, (C) IFNλ, and (D) IFNω were observed in response to PB84 constructs displaying 20 or 40 CpG-OHs compared to unmodified 0 CpG-OH PB84, while the addition of 20 or 30 CpG-OHs to ICO42 constructs had minimal effect in some cases and reduced interferon expression levels in others. NANP concentrations were adjusted across samples to ensure constant CpG concentration for all modified constructs. A mixture of ODN2216, lipopolysaccharide, and phytohemagglutinin was used as the assay positive control (pos. con). Each bar represents averaged triplicate data from a single donor,

where n = 3 donors. P values are from a one-sided analysis of variance (ANOVA) with a post-hoc Tukey test to correct for multiple comparisons (*: $P \leq 0.05$; **: $P \leq 0.01$, ***: $P \leq 0.001$, ****: $P \leq 0.0001$). All unlabeled pair-wise comparisons are not significant.